ACS Photonics

Open Access

pubs.acs.org/journal/apchd5

Article

On the Potential of Optical Nanoantennas for Visibly Transparent Solar Cells

Wayesh Qarony,[§] Mohammad Ismail Hossain,[*,§] Asman Tamang,[§] Vladislav Jovanov, Md. Shahiduzzaman, Md. Shamim Ahamed, Ragip A. Pala, Alberto Salleo, Yuen Hong Tsang, and Dietmar Knipp

Cite This: *ACS Photonics* 2023, 10, 4205−4214

Read Online

ACCESS | Metrics & More | Article Recommendations | Supporting Information

ABSTRACT: This study aims to determine the maximum possible energy conversion efficiency of visibly transparent solar cells using the detailed balance limit (also known as the Shockley−Queisser limit) and compare it to the efficiency of traditional single-junction solar cells. To achieve this, a new optical nanoantenna has been designed to absorb incoming light selectively, enhancing the average visible transmission while maintaining high absorption in the infrared and UV regions. The color appearance of the antennas has also been evaluated through colorimetrical characterization. Our findings indicate that it is possible to achieve high average visible transparency and energy conversion efficiency of over 80 and 18%, respectively, by carefully selecting semiconductor materials. Such solar cells are versatile enough to be integrated seamlessly into smart windows, agrivoltaic concepts in open and protected cultivation, mobile devices, and appliances without compromising their appearance or functionality. The dimensions and optics of the proposed antennas and visibly transparent solar cells have been thoroughly discussed.

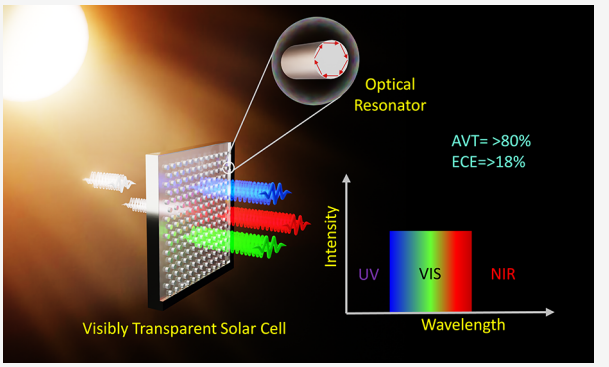

KEYWORDS: *Shockley−Queisser limit, detailed balance limit, FDTD, visibly transparent solar cell, optical antenna, color science*

INTRODUCTION

Uprising energy demand and climate change mitigation have made photovoltaic (PV) solar cells ubiquitous and seamless renewable solar energy harvesting technology in our daily needs. In addition, the steady growth in energy production from photovoltaic solar cells is expected to be one of the primary sources of electrical energy supply while considering it as an alternative energy production technology to fossil fuels. Beyond this pristine functionality of solar cells, there is a considerable interest in integrating them onto the functional surfaces of automobiles, buildings, agriculture, and even space aircraft.[1,2] Lightweight solar cells, flexible solar cells, or visibly transparent solar cells (VTSCs) could be ideal candidates for such applications and architectures.[1,3,4] Interestingly, VTSCs are fundamentally transparent in the visible range of the sun's spectrum, which allows them to be a perfect candidate as on-demand transparent energy generators for integration within architectural surfaces of commonly used low emissivity windows and glass facets buildings, solarium, controlled environment agriculture (CEA) like greenhouses, mobile devices, and sunroofs of automotive or appliances while maintaining their visual appearance and prime functionality. In addition, VTSCs can be achieved by considering strong absorption of both the ultraviolet (UV) and near-infrared (NIR) regions of the solar spectrum exhibiting higher energy conversion efficiency (ECE) than conventional UV solar cells.[2,4] Due to this unique light management property, it can limit harsh effects on humans with skin cancers and eye diseases caused by UV light dictated by its vital photon energy.[5] Also, VTSCs have significant benefits for reducing plant stress, the potential for water savings in the open and closed concept of agriculture, and energy savings for CEA applications. Furthermore, VTSCs can be combined with the low emissivity windows. Low emissivity windows are transparent in the visible part of the optical spectrum, while the window reflects infrared and long-wave thermal radiation. According to the CIE (International Commission on Illumination), the visible (VIS) spectrum ranges (also known as photosynthetically active radiation (PAR) for plant photosynthesis and averaged visible transmission (AVT) band from ∼400 to ∼700 nm, or from 3.2 to 1.8 eV.[6,7] The CIE sets illuminant standards and describes the human vision

Received: July 5, 2023
Revised: November 1, 2023
Accepted: November 2, 2023
Published: November 28, 2023

system, commonly called the standard observer.[6] The function of a conventional low emissivity window could be altered by converting the NIR radiation into electrical energy, where the radiation from 1.8 eV to E_G (E_G is the band gap of the absorber for realizing the VTSC) with <1.8 eV can be absorbed by the VTSC and photons with energies smaller than E_G must be reflected.

Hence, the combination of VTSC and low emissivity windows will allow us to generate more electrical energy with a maximal surface coverage of the windows. Designing such a configuration is complicated; hence, our study introduces the VTSC built from resonant optical antennas (resonators) made of optimal materials. This configuration can regulate light propagation by altering the resonators' properties, covering the entire VIS area while generating electricity from UV and NIR regions. A schematic representation of the VTSC using optical resonators prepared on a transparent surface like the window and greenhouse glazing is shown in Figure 1. More detailed information on the device design is provided in the following section.

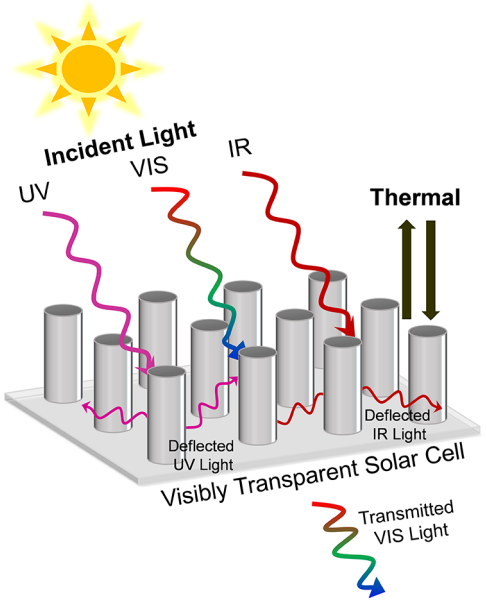

Figure 1. Schematic representation of a visibly transparent solar cell (VTSC) based on an optical resonator integrated into a transparent surface.

Device Architecture of VTSCs and Optical Antennas. Different concepts for building VTSCs have been proposed and implemented.[8−12] Most of the VTSCs are based on organic materials.[9−11] Furthermore, most authors use donor−acceptor heterojunction solar cells.[8−10] The selected materials exhibit absorption bands in the NIR. On the other hand, the electronic structure of an inorganic semiconductor used for realizing a conventional solar cell (Conv-SC) is typically characterized by extended density of states (DOS), which follow a square root dependence, as shown in Figure 2a. A direct band-to-band transition absorbs photons with photon energies larger than E_G. The DOS of organic materials is commonly approximated by Gaussian distributions for the HOMO (highest occupied molecular level) and LUMO (lowest unoccupied molecular level) levels, as depicted in Figure 2b. Hence, the optical properties are determined by the

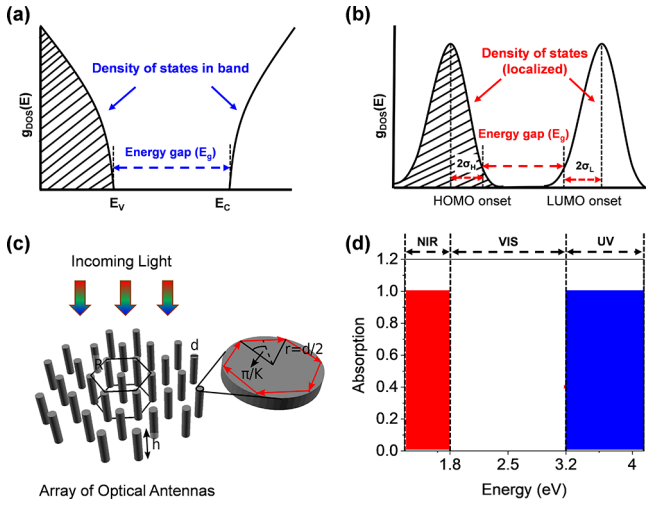

Figure 2. (a) Density of states (DOS) of inorganic material with extended DOS. (b) Gaussian DOS of an organic semiconductor. (c) Schematic sketch of optical antennas in a hexagonal arrangement. (d) Maximum ideal-like light absorption in the proposed array of optical resonators arranged in a hexagonal grid.

energy difference between the HOMO and LUMO levels and the width of the DOS. In addition, materials with well-defined optical properties are required to realize transparent solar cells with high ECEs. The materials must be optimized by molecular engineering and organic synthesis. Besides organic materials, it might be possible to realize and optimize resonant optical structures or optical nanoantennas by tailoring the properties of inorganic materials. Metasurfaces consisting of subwavelength large 2D or 3D optical resonators allow for tailoring of the optical properties. Figure 2c shows the schematic representation of the cylindrical-shaped resonant optical antennas in a hexagonal arrangement. The optical resonator is defined by the antenna diameter (d), antenna height (h), and spacing between antennas (R). The antennas support whispering gallery or leaky modes,[13−15] where the circular boundary of the optical resonator repeatedly reflects the light. The resonance condition for an optical resonator with a diameter d can be described by $m \cdot \lambda_{eff} = K \cdot d \cdot \sin(\pi/K)$, where m is the order of the resonance, λ_{eff} is the effective wavelength at which resonance is observed, and K is the number of reflections at the circular boundary.[14−16] For $K \rightarrow \infty$, the resonance conditions simplify to

$$m \cdot \lambda_{eff} \approx \pi \cdot d \quad (1)$$

From eq 1, it follows that the antenna diameter can control the resonance conditions of the resonator.

Furthermore, if the resonant condition is achieved for the first-order mode (HE_{11}) at wavelength λ_0, it will also be achieved for the second-order mode (HE_{12}) at $\lambda_0/2$, third-order mode (HE_{13}) at $\lambda_0/3$, and so on. In other words, d of the antennas can be varied to tune the fundamental transverse resonance mode HE_{11} for a chosen wavelength. In contrast, the transverse mode defines the primary transparency gap HE_{12}.[17,23] To utilize resonant optical structures for the realization of VTSCs effectively, the transparency gap between the HE_{11} and HE_{12} resonance modes must overlap with the VIS region of the electromagnetic (EM) spectrum. Under such restrictions, the absorption peaks of HE_{11} and HE_{12} would be located in the NIR and UV regions of the EM spectrum, respectively. Figure 2d displays the maximum ideal-like

https://doi.org/10.1021/acsphotonics.3c00932
ACS Photonics 2023, 10, 4205−4214

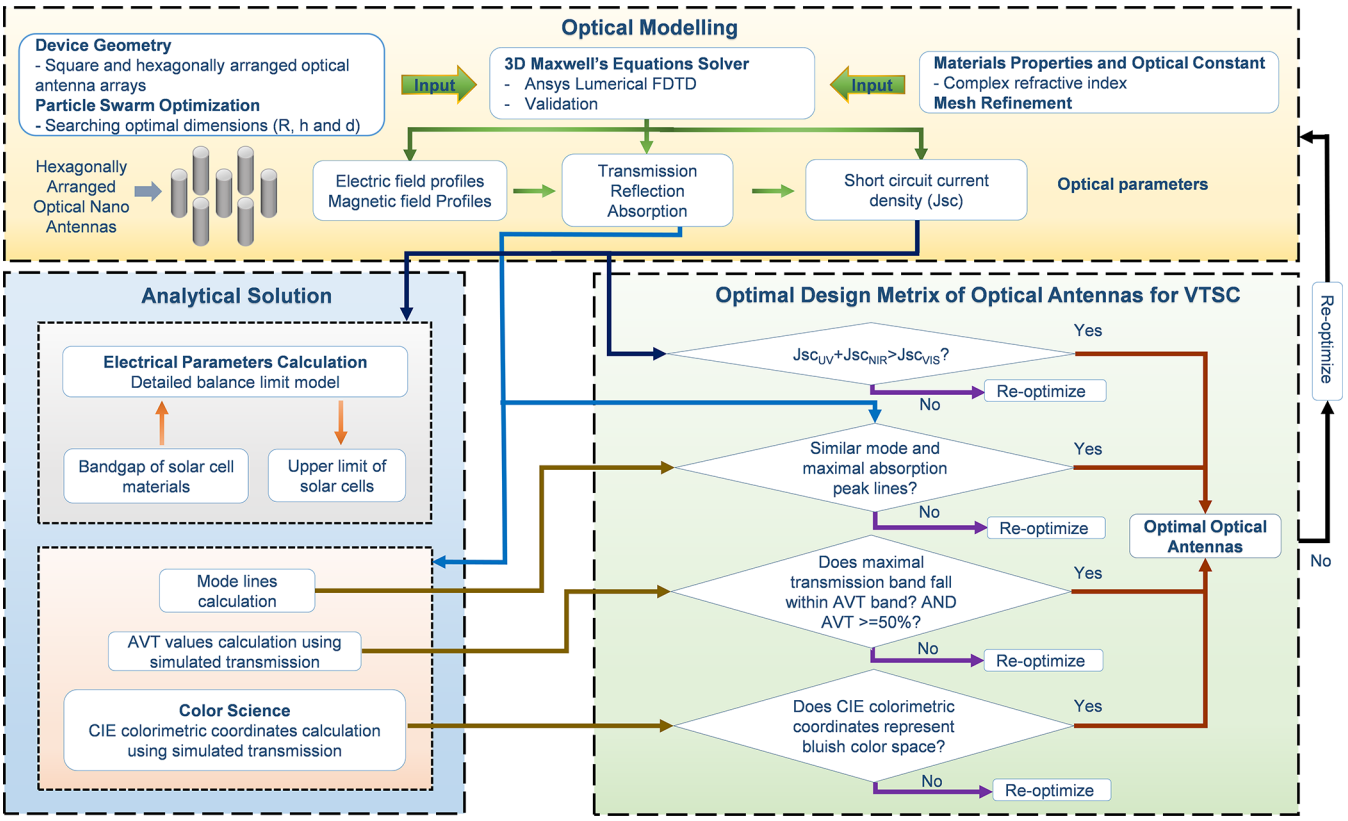

Figure 3. Process flow diagram for designing optical antenna-based VTSCs. First, 3D optical simulations and the PSO algorithm are conducted for optical antennas with various geometries to get EM fields. Second, different analytical solutions are studied to calculate electrical parameters of solar cells, mode lines, AVT values, and CIE colorimetric coordinates. Finally, simulated and calculated optical and electrical parameters are compared to design optimal optical antennas, which can be incorporated for realization of VTSCs.

absorption of hexagonally arranged resonant optical antennas, exhibiting unity absorption or zero transmission in NIR and UV regions; on the other hand, zero or partial absorption or unity transmission in the VIS region. Furthermore, the solar cell design with the resonant antennas has to be optimized to achieve maximum average transparency, or AVT, in the visible range of the wavelength spectrum based on the need of particular applications for conventional and agricultural buildings and simultaneously maximum light absorption in the UV and NIR (Figure 2c,d). To achieve this goal, it is necessary to systematically optimize the dimensions of the optical resonators as well as the material properties of the optical resonators. Our study focuses on a linear architecture that employs optical antennas for the VTSC while eliminating the need for solar-concentration elements, such as luminescent solar concentrators or quantum dot concentrators. The VTSC is positioned directly in the path of the incident light, and its device architecture is designed to match traditional solar cells. This makes transferring the technology to a large area of VTSCs feasible without redesigning the solar cells.

Methodology and Optimization Considerations. Realizing efficient VTSCs requires a complete understanding of the optical and electrical properties of materials used for resonant optical antennas, requiring a detailed optimization process. A full range of optimization processes of optical antenna-based VTSCs involves several crucial steps, such as rigorous optical simulations, numerical validations, analytical solutions, and design metrics analysis, in conjunction with the CIE color science study. Figure 3 shows a process flow diagram to conduct these investigations for designing optical resonators and developing VTSCs. In this study, rigorous 3D electromagnetic (EM) simulations of differently arranged optical antennas were performed using Ansys Lumerical FDTD,[18] a commercial Maxwell's equation solver embedded with the particle swarm optimization (PSO) algorithm,[19] to attain the initial optimization condition of the resonator for a wide range of materials. The adapted simulation tool can carry out parametric sweeping of any arbitrary shapes or geometries covering a broadband spectrum, also providing a good agreement with the experimental results.[20−22] The complex refractive indices of materials are used as inputs for the optical simulations provide electric field distributions and power density profiles within antenna structures and their surroundings.[22,23] This, in turn, enables the calculation of the absorption and short-circuit current density (J_{SC}) along with transmission and reflection. A detailed description of the simulation process and setup is provided in the Supporting Information (S1). To further understand the numerical approach's effectiveness, a simulation outcome validation with the theoretical results is presented in the Supporting Information (S2, Figures S1 and S2). Subsequently, detailed balance (DB) theory was used to model the upper limit of the investigated VTSCs and estimate electrical characteristic parameter values for the studied devices. Afterward, the simulated transmission spectra were utilized to calculate the AVT of the antenna within the AVT band and the CIE color coordinates and color patches of the antennas. Finally, the practical materials' properties of well-known solar cells were used to further explore the potential of optical antennas, which can be incorporated for the realization of VTSCs.

https://doi.org/10.1021/acsphotonics.3c00932
ACS Photonics 2023, 10, 4205−4214

RESULTS AND DISCUSSION

Material properties and antenna arrangement significantly influence the optics of VTSCs. A constant complex refractive index describes the optical antenna material N ($N = n + j{\cdot}k$), where n is the refractive index and k is the extinction coefficient. During the initial stage of this study, an optimization process was conducted process for various n (real part of N) values that range from 1.5 to 5.5 by keeping the k (imaginary part of N) value constant ($k = 0.2$) to cover a wide range of material systems, including Ge, Si, III−V materials, and perovskites. The goal was to identify an ideal material system that could provide the optical response for developing VTSCs. Figure S3 in the Supporting Information shows the influence of the complex refractive index on the absorption of hexagonally arranged optical antennas. The optimized complex refractive index (N) is 3.5 + $j{\cdot}$0.2. The optimized refractive index leads to a maximum absorption at 350 and 780 nm wavelengths, while minimal absorption is achieved in the 425−600 nm wavelength range. The resonance conditions of an optical resonator with a diameter d can be defined by eq 1, and spacing (R) between optical antennas larger than the antennas' height ($R \gg d$). Therefore, optimizing d plays a crucial role in the performance of optical antenna-based VTSCs. To understand the influence of d on the optical properties of the optical antennas and their array arrangements, the antenna diameter (d) initially varied fixed h and R values. Figures S3 and S4 in the Supporting Information demonstrate the absorption, transmission, and reflection of optical antennas arranged in square and hexagonal grids, while antenna diameters varied from 70 to 150 nm. A blue shift of the absorption peaks occurs while decreasing the antenna diameter. Interestingly, the hexagonally arranged antenna array exhibits higher absorption than the square grid antennas. However, both arrangements show almost similar reflections. Thus, these findings led to further investigation of only hexagonally configured resonators. The antenna spacing (R) is tuned from 340 to 750 nm to find the desired absorption peaks, while the antenna diameter is varied from 70 to 240 nm. The combined effect on the optical properties of optical antennas is presented in Figure S6 in the Supporting Information. To achieve optimal control over absorption, transmission, and reflection in the visible spectrum, it is vital to optimize the profile dimension or geometry of the resonator over a wide range.

Absorption and transmission maps for different dimensions of optical antennas are provided in Figure S7 in the Supporting Information. Controlling the diameter of optical antennas is important for optimizing optical antenna-based VTSCs, which can be achieved by considering the resonance conditions and hybrid modes described above. The absorption map of optical antennas by varying d of the antenna against the incident wavelength is shown in Figure 4d. These absorption phenomena can be described through mode theory, where leaky mode resonances cause absorption peaks in the map. These leaky modes are hybrid modes characterized by magnetic and electric components and can be labeled by $HE_{m,n}$, where m is the order and n corresponds to the radial mode number. Mode profiles for different orders are presented in Figures S8−S10 in the Supporting Information. The absorption map and mode profiles illustrate absorption resonance peaks and hybrid resonance modes, respectively. A strong absorption resonance occurs in the lowest hybrid mode

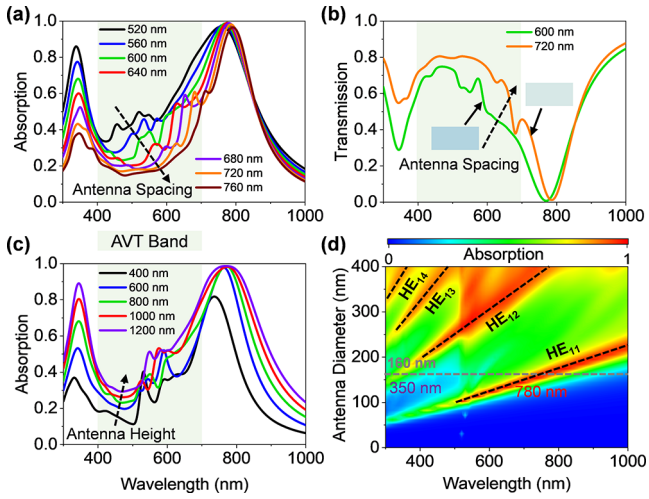

Figure 4. (a) Influence of antenna spacing (R) on the absorption of the optical antenna array for fixed height (h) = 800 nm and diameter (d) = 160 nm of antennas. (b) Transmission for antenna spacing of 600 and 720 nm as a function of wavelengths, keeping the height and diameter of the antennas as 800 and 160 nm, respectively. Color patches of the optical antennas for simulated transmission are shown as insets in (b). (c) Influence of height of optical antennas as a function of wavelengths for R = 600 nm and d = 160 nm. (d) Absorption map of optical antennas as a function of wavelengths and diameter for a fixed h = 800 nm and R = 600 nm. The gray dash line represents absorption for the diameter of 160 nm, exhibiting absorption peaks at wavelengths of 350 and 780 nm.

(HE_{11}) for the smaller diameter antennas within the entire spectrum range. On the other hand, resonance modes such as HE_{12}, HE_{13}, and HE_{14} are also observed for larger diameters of antennas in the shorter wavelength region. In this study,the optimal antenna diameter is found to be 160 nm, which exhibits absorption peaks in both UV and NIR regions while showing less absorption and maximized transmission in the VIS spectral window (400−700 nm), as shown in Figures 4 and S7 in the Supporting Information. Simulated absorption and transmission of hexagonally arranged antenna array are exhibited in Figures 4a, S7a and S7b in the Supporting Information for varying antenna spacing (R), ranging from 160 to 1000 nm. It is observed that two absorption peaks appear in the NIR at ∼780 nm (1.6 eV, HE_{11}) and UV at 350 nm (3.5 eV, HE_{12}) regions that allow the resonant wavelengths to correspond to absorption peaks. This satisfies the simplified resonance condition given in eq 1. The absorption region between these two peaks defines the solar cell's AVT. The spacing between the antennas controls the wavelength region in which the solar cell is transparent. The visible transparency of the device is confirmed by the transmission plots, as shown in Figure 4b, for antenna spacings of 600 and 720 nm. A similar characteristic can be pronounced by varying the height of the antennas, as presented in Figures 4c, S7c and S7d in the Supporting Information, where absorption peaks in both UV and infrared regions are increased with increasing antenna height. In addition, the influence of antenna dimensions on the VTSC's optics is further extended in Figure S11 (Supporting Information). Such a detailed optimization of the geometries of optical antennas helps to improve the AVT of incident light and also enhance the ECE of VTSCs. The AVT values and current densities are calculated for respective simulated transmission and absorption for different dimensions of the

https://doi.org/10.1021/acsphotonics.3c00932
ACS Photonics 2023, 10, 4205−4214

optical antennas. Figure 5 shows the influence of antenna diameter, spacing, and height on the calculated AVTs for desired spectral window (400−700 nm) and illustrates them for AM 1.5G and AM 0 spectral irradiances along with the current densities in VIS and combined UV and NIR regions. The effect of antenna spacing for the given height and diameter is presented in Figure 5a, b for AM 1.5G and AM 0 sunlight intensities.

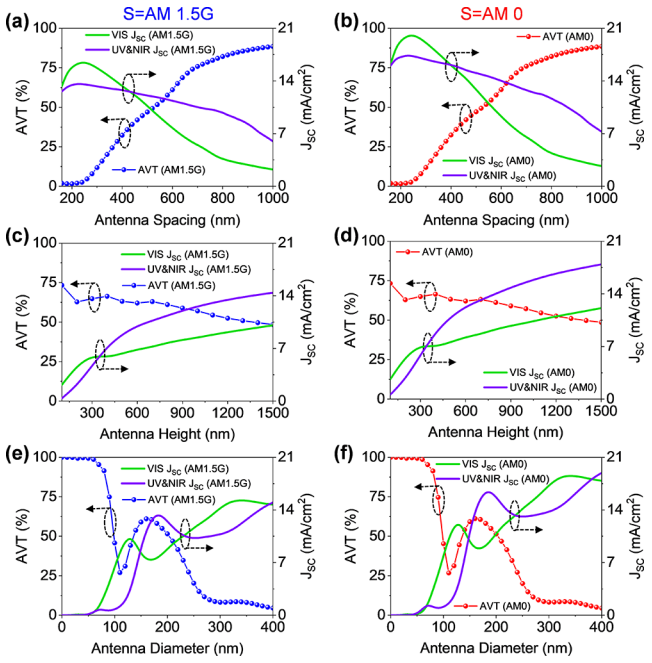

Figure 5. Calculated AVTs of the optical antennas along with the J_{SC}s in the sun's different spectral regions while varying the (a, b) antenna spacing, (c, d) antenna height, and (e, f) antenna diameter for the spectral intensity of (a, c, e) AM 1.5G and (b, d, f) AM 0.

The AVT drops for a solar cell with a small spacing and vice versa. A resonant antenna with optimized spacing may allow over 80% average transmission in the VIS region with maximum absorption of incident light approaching 100% in the NIR region, as shown in Figure 4b. Furthermore, color patches of the optical antennas for simulated transmission are shown as insets in Figure 4b. The color patches represent the bluish appearance of the VTSC based on optical antennas. The corresponding calculated color indices are included in Table S1 in the Supporting Information, and their calculation process is explained elsewhere.[24,25] The high absorption within the NIR also reduces the space cooling loads in buildings and greenhouses because the spectrum with the NIR range increases thermal loads without having any benefits in their prime function. The antenna height (h) and diameter (d) also play an important role in the solar cells' AVT and current densities. Overall, it is observed that J_{SC}s of AM 0 are higher than AM 1.5G J_{SC}s, but their AVTs are almost identical, indicating that the sun intensity has no influence on the AVT. Also, the average reflection in the VIS region was calculated while changing the dimensions of optical antennas, as listed in Table S2 in the Supporting Information. The details of the calculations of AVT are provided in Supporting Information (S3).[23]

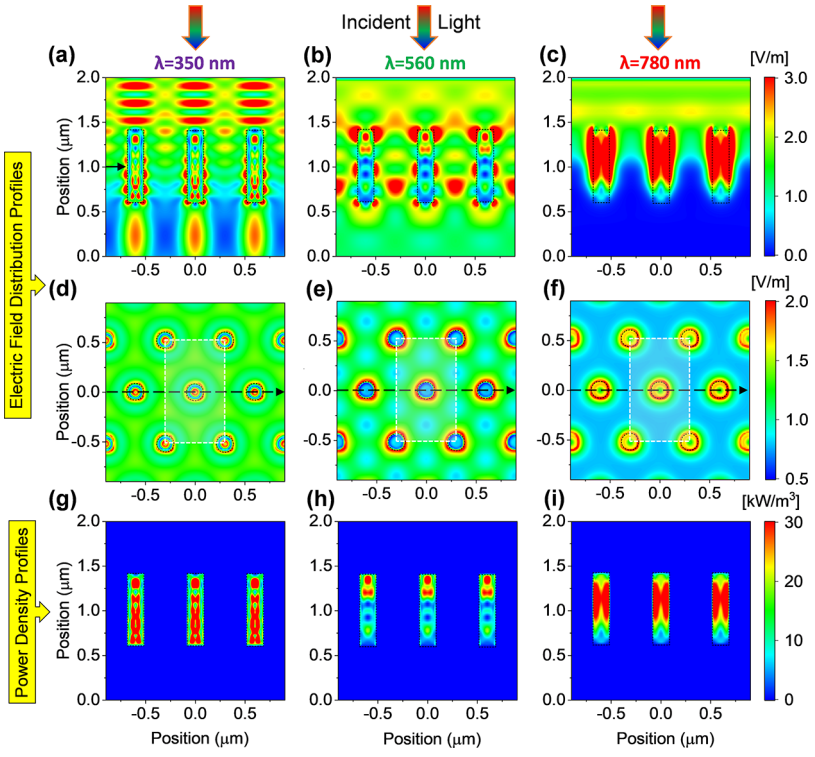

Figure 6. Simulated electric field distribution of the hexagonally arranged antennas under monochromatic illumination of wavelength (a,d) 350 nm (UV), (b,e) 560 nm (VIS), and (c,f) 780 nm (NIR), where diameter is 160 nm, height is 800 nm, and spacing is 600 nm. Corresponding simulated power densities under monochromatic illumination of wavelength (g) 350 nm (UV), (h) 560 nm (VIS), and (i) 780 nm (NIR). Side-views of the electric fields distributions and power densities as indicated by black arrows in (d−f) are shown in (a−c). Top-views of the electric field distributions as indicated by black arrows in (a−c) are shown in (d−f).

https://doi.org/10.1021/acsphotonics.3c00932
ACS Photonics 2023, 10, 4205−4214

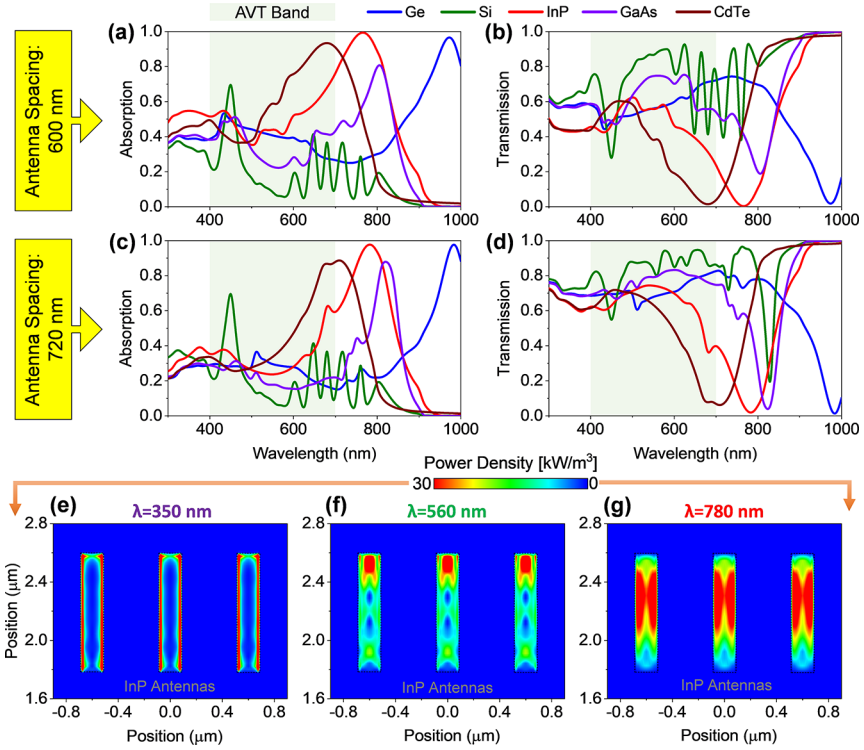

Figure 7. Absorption and transmission of optical antennas based on various photovoltaic materials as a function of wavelengths for the antenna spacing of (a, b) 600 and (c, d) 720 nm, respectively. The time-averaged power density profiles of the InP antenna under the monochromatic wavelength of (e) 350, (f) 560, and (g) 780 nm, respectively. The antenna height is 800 nm, diameter is 160 nm, and spacing is 600 nm.

In our continued study of the optics of VTSCs based on the optimized optical antenna, the electric field distributions and power absorbed densities across the antenna array for different illumination wavelengths are calculated, as shown in Figure 6. The details of these calculations are provided in the Supporting Information (S1).[26] Figure 6a–c and g–i visualizes the calculated time-averaged electric field distributions and power absorbed densities, respectively, along the center (*xz*-direction) of the hexagonally arranged optical antennas under a monochromatic illumination of 350, 560, and 780 nm. Top view of the corresponding electric field profiles is shown in Figure 6d–f. A high absorption characteristic along the antenna in both NIR (λ = 780 nm) and UV (λ = 350 nm) regions is observed due to the enhanced optical coupling of fundamental and higher-order modes along the antennas.

However, it is worth noting that for the incident wavelength of 560 nm (VIS region), the light does not couple to the antenna efficiently due to the absence of an optical mode as compared to that for wavelength of 350 and 780 nm. This is also confirmed by the absorbed power density profiles of the antenna shown in Figure 6g–i. For the shorter wavelength (λ = 350 nm) defined by HE_{12} mode, the light absorption is highly pronounced along the length of the optical antenna exhibited in Figure 6a,d,g. On the other hand, the absorption in the longer wavelength (λ = 780 nm) is relatively more distinct in the antenna, as presented in Figure 6c,f,i. A notable EM field distribution along the wire (Figure 6c,f) leads to maximum light absorption. This high absorption phenomenon is caused by the generation of HE_{11} optical modes throughout the length of the wire, as shown in Figures 4d and 6c,f,i. In contrast, for the VIS wavelength region (λ = 560 nm), the guided optical modes reduce abruptly upon incidence on the optical antennas, and they cannot reach all the way to the end of the resonator, resulting in the absorption of light of only about 80 nm of the wire from the top of the surface as presented in Figure 6b,e,h. The calculated time-averaged power densities and electric field distributions across the center (*yz*-direction) of the hexagonally arranged antennas and their surroundings under monochromatic wavelengths of 350, 560, and 780 nm are provided in Figure S12 in the Supporting Information. As compared to power densities in the *xz*-direction, a similar optical phenomenon can be observed in the case of power densities in the *yz*-direction that validate the uniform distribution of incident waves. Furthermore, the potential of the proposed design approach of optical resonant antennas with a set of realistic material systems (Ge, Si, GaAs, InP, and CdTe) is studied. Figure 7a–d shows the absorption and transmission for optical antennas built from different solar cell materials. Simulated reflection and reflection losses of antennas prepared with these materials are shown in Figure S13 in the Supporting Information. In the case of InP-based optical antennas, desired absorption and transmission spectra are realized, which are also confirmed by the corresponding power density profiles presented in Figure 7e–g. In addition to that, a comparison between spectral densities of ideal and InP-based optical antennas is presented in Figure S14. Interestingly, there is a trade-off between the ECE and the AVT of solar cells. In comparison, experimentally realized VTSCs exhibit ECEs of about 12.6% in organic–inorganic halide perovskite-based devices, while the maximum AVT of such devices could be only about 20%.[27,28]

However, emerging and ubiquitous renewable energy solutions cannot be realized with such a low AVT. At this point, the upper theoretical limit of the ECE and the optimal band gap of a material used to realize VTSCs are imperative to study. Detailed balance (DB) limit calculations, commonly

https://doi.org/10.1021/acsphotonics.3c00932
ACS Photonics 2023, 10, 4205–4214

called Shockley−Queisser (SQ) limit calculations, are used to determine the upper limit of the ECE of solar cells.[29,30] Only the bandgap is used as the input parameter to calculate the upper limit of the ECE of the solar cells. Parameters describing the electrical or optical properties of the used semiconductor, such as the diffusion length and the penetration depth, are not considered. Hence, the DB calculations cannot be used to derive the optimal device design directly. Nevertheless, several authors tried to expand the DB limit model by considering the electronic and optical of the solar cell.[31] However, we stick to classical DB theory in the following. The maximal J_{SC} of a solar cell as a function of the band gap of the used semiconductor can be calculated by

$$J_{SC} = \frac{q}{F}\int_0^{\infty} \phi_{Sun}(E) \times A(E)\mathrm{d}E \tag{2}$$

where J_{SC} is the short-circuit current density, F is the area of the solar cell, q is the elementary charge, E is the photon energy, $\phi_{Sun}(E)$ is the photon flux of the sun, and $A(E)$ is the absorption of the solar cell. The absorption is given by $A(E)= H(E-E_G)$, where $H(E)$ is the Heaviside function and E_G is the band gap of the absorber material. The absorption $A(E)$ is equal to one for $E \geq E_G$ and equal to zero for $E < E_G$. J_{SC} is determined by integrating from zero to infinity. Equation 2 can be rewritten to calculate J_{SC} by

$$J_{SC} = \frac{q}{F}\int_{E_L=E_G}^{E_H} \phi_{Sun}(E)\mathrm{d}E \tag{3}$$

In the case of a conventional broadband solar cell (Conv-SC), E_L is equal to E_G, and E_H is equal to infinite, while in the case of a VTSC, $E_H \cong 1.8$ eV. The absorption of a VTSC is shown in Figure 8b, while the spectral irradiance of sunlight for AM 0 and AM 1.5G is illustrated in Figure 8a. We considered standard AM 0 and AM 1.5G spectral irradiances to calculate all solar cell parameters. AM 0 corresponds to the sun spectrum outside the atmosphere (zero atmospheres), approximated by the 5800 K blackbody. AM 1.5 G corresponds to the global spectrum of the sun after passing the atmosphere of the earth at an angle of 48° (1.5 = 1/cos(θ), θ = 48°). AM 1.5G is commonly used to determine solar cells' ECE. The calculated J_{SC} of Conv-SC and VTSC is shown in Figure 8c. The sunlight up to 1.8 eV accounts for an upper J_{SC} of 19.01 mA/cm^2. Hence, this amount reduces the total J_{SC} of a VTSC. The FF and V_{OC} of the Conv-SC and VTSC are shown in Figure 8d,e, respectively. The modified absorption of the solar cell has only a small effect on the FF and V_{OC}. The theoretical limit of the ECE is shown in Figure 8f. A Conv-SC exhibits a maximal ECE of approximately 30% using semiconductors with an optimal bandgap of 1.2−1.4 eV, whereas the VTSC exhibits an upper limit of the ECE of 18%, while the optimal bandgap of the absorber is approximately 1.0 eV. Hence, a VTSC can still generate up to 50% of the energy of a conv-SC. To achieve the maximal ECE, the solar cell absorber is required to follow with absorption, $A(E) = 0$ for 3.1 eV < E < 1.8 eV and absorption, $A(E) = 1$ from 1.8 eV < E < 1.0 eV.

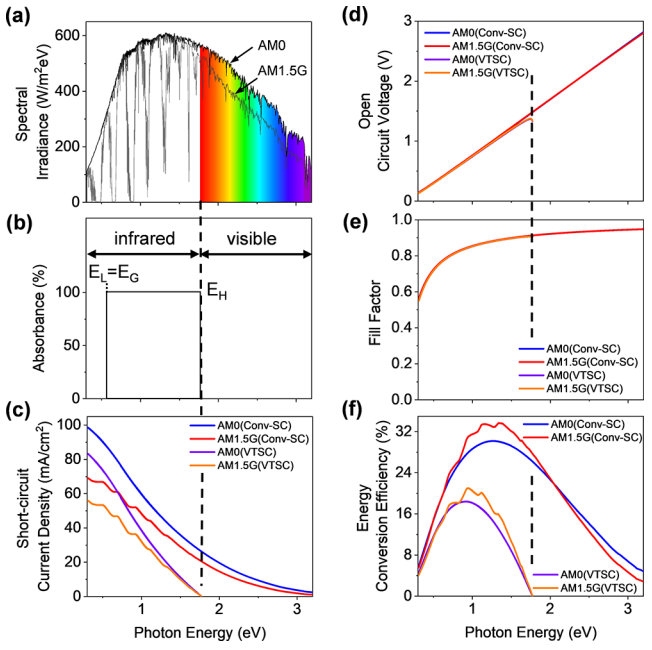

Figure 8. (a) Spectral irradiance of the sun at AM 0 and AM 1.5G. The theoretical limit of (b) photon absorption, (c) short-circuit current density (J_{SC}), (d) open-circuit voltage (V_{OC}), (e) fill factor (FF), and (f) ECE of the conventional solar cell (Conv-SC) and VTSC as a function of photon energy (material's band gap).

Various real solar cell materials such as Ge, Si, InP, GaAs, and CdTe were subjected to optical simulations to determine their AVTs and J_{SC}s. These values were then used as inputs for the DB theory to create electrical characteristic parameters for solar cells. The ECEs of VTSCs were estimated using these parameters. Table 1 provides a summary of the AVTs and photovoltaic parameters of VTSCs simulated from different materials, with antenna spacings of 600 and 720 nm for AM 1.5G. Based on the optimized design, Si shows more than 84% transparency in the VIS spectrum. However, the ECE of Si-based VTSC was only 2.74%. In contrast, CdTe-based VTSC (R = 600 nm) exhibits the highest efficiency of over 18%, but its AVT is limited to only 33.7%. It is essential to maintain a trade-off between AVT and ECE of VTSCs, as stated earlier. Our investigation revealed that InP could be a suitable material for the realization of VTSCs. The optical antenna built from

Table 1. Simulated Optical and Electrical Parameters of Solar Cells Prepared with Different Photovoltaic Materials and Corresponding Band Gaps[a]

Solar Cell Material	E_g (eV)	AVT (%)	J_{SC} (mA/cm²)	V_{OC} (V)	FF	ECE (%)	CIE Color Patch
Antenna Dimension: R=600 nm, d=160 nm, and h=800 nm							
Ge	0.67	58.06	16.03	0.45	0.780	5.62	
Si	1.12	72.74	5.90	0.84	0.860	4.26	
InP	1.27	48.92	18.6	0.98	0.880	16.04	
GaAs	1.43	62.63	13.25	1.13	0.890	13.33	
CdTe	1.5	33.70	17.32	1.19	0.895	18.4	
Antenna Dimension: R=720 nm, d=160 nm, and h=800 nm							
Ge	0.67	71.65	11.80	0.45	0.78	4.14	
Si	1.12	84.06	3.79	0.84	0.86	2.74	
InP	1.27	64.01	14.72	0.98	0.88	12.70	
GaAs	1.43	76.24	10.24	1.13	0.89	10.30	
CdTe	1.5	51.23	13.92	1.19	0.895	14.82	

[a]The AVTs and CIE color patches for different solar cell materials are calculated based on the simulated transmission of hexagonally arranged antenna arrays. The simulations consider two different antenna spacings (R = 600 and 720 nm) and an antenna diameter of 160 nm and height of 800 nm.

https://doi.org/10.1021/acsphotonics.3c00932
ACS Photonics 2023, 10, 4205−4214

InP demonstrated a high ECE ranging from 12.7 to 16.04% and reasonable AVT ranging from 49 to 64%. Table 1 also includes the CIE Color patches of VTSCs for optical antennas made from different materials. Corresponding colorimetric indices for determining color patches for different photovoltaic materials with antenna spacing of 600 and 720 nm are listed in Tables S3 and S4. Besides understanding the effect of sunlight intensity variation (e.g., AM 1.5G and AM 0), as presented in Figure 5, a series of investigations have been conducted to realize the external factors such as incident light angle, surrounding environment of the optical antenna, and impact on the VTSC performance, so that the study can contribute to the broader understanding of the technology's adaptability. In this study, InP was selected for the optical antenna material. Figure S15 in the Supporting Information demonstrates the influence of incident light angle on the solar cell's absorption, transmission, and J_{SC}. J_{SC}s of VTSCs in the case of AM 1.5G and AM 0 sunlight intensities decreased from 18.6 to 9.07 and 22.45 to 11.46 mA/cm^2, respectively, for incident angle varying from 0° to 75°. Simulated absorption and transmission further support the changes in J_{SC} of VTSCs for varied incident angle. In the next study, optical simulations are performed to assess the environmental condition of the VTSCs by considering two cases: (A) the optical antennas are surrounded by air medium (n = 1) and (B) optical antennas are encircled by SiO_2 (n = 1.4∼1.5). Our findings demonstrate that Case B exhibits more interferential effects than Case A, resulting in multiple ripples in its corresponding absorption and transmission spectra. However, the antenna environment does not significantly influence the generated J_{SC}, as shown in Figure S16. J_{SC} of Case B drops by less than 1% for both sunlight intensities compared to Case A. Such optical phenomena can be further confirmed by their corresponding electrical field distribution profiles for a monochromatic wavelength of 350 and 780 nm for Cases A and B, as depicted in Figure S16c,d.

Finally, this study proposes VTSC, a new type of solar cell based on classical physics principles and built from resonant optical antennas. Using the FDTD method in 3D, the optics of VTSCs and obtained important metrics such as generation rate, power density, transmission, absorption, reflections, quantum efficiency, short-circuit current density, and unwanted parasitic losses are analyzed. A detailed optimization process is conducted to maximize the performance of optical antennas by varying their geometric dimensions for VTSCs. At the same time, the widely used classical DB theory was used to estimate electrical characteristic parameters of solar cells. Moreover, though classical physics principles form a strong basis for comprehending different aspects of optical antenna-based VTSCs, quantum physics principles may be essential in the future for fully understanding the behavior of resonators at the nanoscale owing to the impact of quantum effects. Likewise, to achieve high J_{SC} and ECE, materials with multiple optical resonances are essential. Organic composite materials or metasurfaces with optical antennas could be utilized. Anomalous dispersion or low refractive index materials in UV and VIS can also increase J_{SC} and ECE. Combining these approaches with organic materials could be promising, although controlling spectral properties might be challenging due to the low refractive index.

Regarding the experimental realization of such solar cells built from optical antennas (e.g., InP), several fabrication techniques, such as solvothermal process,[32] metal-assisted etching,[33] metal−organic vapor phase epitaxy (MOVPE),[34] and molecular beam epitaxy (MBE)[35] techniques, can be employed to fabricate InP optical antennas. Selective-area MOVPE or MBE methods can be utilized for growing InP nano antennas, with dopant control allowing for axial growth in a $p-n$ or $p-i-n$ configuration, depending on the design of the solar cells.[33,35] To fabricate such nano antennas, traditional lithography processes such as nanoimprinting or e-beam lithography can be used to pattern and control the antenna diameter.[33,35−37] This can be followed by dry etching (RIE/ICP) or metal deposition using techniques such as ALD, e-beam, or Sputter with a lift-off method. Transparent conductive oxide (ITO) can then be sputtered as an electrode, and the space between optical antennas can be filled with a transparent material like polymer. Finally, another transparent electrode can be deposited on the backside of the InP substrate to complete the device process engineering. The proposed VTSCs can be efficiently integrated with various substrates like glass, Si, PET, etc., depending on the economic viability. Using lithography-based processing, careful and accurate patterning is essential to maintain the trade-off between visible transparency (AVT) and ECE while integrating with different types of substrates.

SUMMARY

This study calculates the upper limit of the energy conversion efficiency of VTSCs (∼18.4%) using the detailed balance (DB) calculation, representing approximately half the upper theoretical limit of conventional single-junction solar cells. The optimal bandgap of traditional solar cells is 1.3 eV, while a shift of the optimal bandgap to approximately 1.0 eV is observed for VTSCs. The realization of VTSCs is complex, and material innovations are required to approach the energy conversion limit. All experimentally realized VTSCs using a linear system architecture are based on organic materials. Herein, we propose an alternative route by using resonant optical antennas. The diameter of the resonant antenna controls the absorption peak and the average visible transparency of the solar cells. Such an optimized resonant antenna may allow over 80% average transmission in the VIS region, with maximum absorption of incident light approaching 100% in the NIR region. This study has shown that it is possible to realize an AVT of >80% with an ECE of >18%. Hence, it is believed that the proposed VTSC has the potential to be a game changer in the modern world and allow a wide range of applications, including buildings, health and security, electronics, agriculture, autonomous vehicles, 5G technology, etc. The successful integration of VTSCs in any controlled environment spaces (building, greenhouse, vehicles) will enhance the potential of the clean energy targets and reduce the cooling loads, reducing carbon emissions from air conditioning systems with reduced cooling loads. VTSCs will also have a massive impact on creating a food-energy-water nexus in agricultural applications (agrivoltaics) with clean energy generation and better crop yields by providing optimal PAR light with minimal water utilization.

ASSOCIATED CONTENT

Supporting Information

The Supporting Information is available free of charge at https://pubs.acs.org/doi/10.1021/acsphotonics.3c00932.

Optical simulation method; validation and analytical solutions (Mie Scattering Theory); influence of

https://doi.org/10.1021/acsphotonics.3c00932
ACS Photonics 2023, 10, 4205−4214

refractive index of resonators on the absorption; effect of antenna diameter on absorption, reflection, and transmission for square-based and hexagonal-based resonators; effect of antenna profile dimension; mode profiles; hexagonal antenna array's optical properties; average visible transmission calculation; simulated power densities and electric field profiles along the center of the hexagonally arranged nanowires under monochromatic illumination; average visible reflection loss, colorimetric indices for antenna patch; comparison spectral densities between ideal and practical devices; effect of the incident light angle; and environment conditions in VTSC performance (PDF)

AUTHOR INFORMATION

Corresponding Author

Mohammad Ismail Hossain − *Department of Applied Physics, The Hong Kong Polytechnic University, Kowloon 999077, Hong Kong; Department of Electrical and Computer Engineering, University of California, Davis, California 95616, United States; Research and Development, Meta Materials Inc. (META), Pleasanton, California 94588, United States;* orcid.org/0000-0003-1290-9329; Email: m.hossain.jub@gmail.com

Authors

Wayesh Qarony − *Department of Electrical Engineering and Computer Sciences, University of California, Berkeley, California 94720, United States; Department of Applied Physics, The Hong Kong Polytechnic University, Kowloon 999077, Hong Kong;* orcid.org/0000-0002-4860-9558

Asman Tamang − *Research and Development, Meta Materials Inc. (META), Pleasanton, California 94588, United States; Research Center for Functional Materials and Nanomolecular Science, Jacobs University Bremen, 28759 Bremen, Germany;* orcid.org/0000-0001-7215-9748

Vladislav Jovanov − *Institute of Chemistry, Technology and Metallurgy, University of Belgrade, 11000 Belgrade, Serbia*

Md. Shahiduzzaman − *Nanomaterials Research Institute, Kanazawa University, Kanazawa 920-1192, Japan;* orcid.org/0000-0002-3092-7793

Md. Shamim Ahamed − *Department of Biological and Agricultural Engineering, University of California, Davis, California 95616, United States*

Ragip A. Pala − *Research and Development, Meta Materials Inc. (META), Pleasanton, California 94588, United States*

Alberto Salleo − *Geballe Laboratory for Advanced Materials, Department of Materials Science and Engineering, Stanford University, Stanford, California 94305, United States*

Yuen Hong Tsang − *Department of Applied Physics, The Hong Kong Polytechnic University, Kowloon 999077, Hong Kong;* orcid.org/0000-0001-5632-5224

Dietmar Knipp − *Geballe Laboratory for Advanced Materials, Department of Materials Science and Engineering, Stanford University, Stanford, California 94305, United States;* orcid.org/0000-0002-7514-3407

Complete contact information is available at: https://pubs.acs.org/10.1021/acsphotonics.3c00932

Author Contributions

[§]W.Q., M.I.H., and A.T. equally contributed to this work. D.K., M.I.H., W.Q., and A.T. conceived the ideas. W.Q. wrote the first draft of the paper. M.I.H. and A.T. revised the manuscript together with R.A.P. and V.J. M.I.H. and A.T. carried out the FDTD model and optical simulations with the support of W.Q. and D.K. M.S., M.S.A., A.S., Y.H.T., and R.A.P. contributed to discussing optics and fabrication of optical antennas. W.Q. proposed the fabrication steps of antennas together with M.I.H. A.T. performed colorimetric characterization for the antenna. D.K., Y.H.T., and M.I.H. supervised the project. All authors discussed the results and commented on the manuscript.

Funding

This work was supported by the Research Grant Council of Hong Kong, Hong Kong (Project number: GRF 152093/18E); the Innovation and Technology Commission of Hong Kong, Hong Kong (Project number: GHP/040/19SZ); the Hong Kong Polytechnic University, Hong Kong (Grant code: B-Q65N, G-YBVG); and Ministry of Education, Science and Technological Development of Republic of Serbia, Serbia (Grant No. 451-03-47/2023-01/200017).

Notes

The authors declare no competing financial interest.

ACKNOWLEDGMENTS

The authors want to thank Mr. Junayed Hossain Rafij (Universiti Tenaga Nasional (UNITEN), Kajang, Malaysia) for software support and graphical image preparation. The authors would like to thank the following funding sources to support the study.

REFERENCES

(1) Bati, A. S. R.; Zhong, Y. L.; Burn, P. L.; Nazeeruddin, M. K.; Shaw, P. E.; Batmunkh, M. Next-Generation Applications for Integrated Perovskite Solar Cells. *Commun. Mater.* **2023**, *4* (1), 2.

(2) Song, Y.; Chang, S.; Gradecak, S.; Kong, J. Visibly-Transparent Organic Solar Cells on Flexible Substrates with All-Graphene Electrodes. *Adv. Energy Mater.* **2016**, *6* (20), No. 1600847.

(3) Makita, K.; Kamikawa, Y.; Mizuno, H.; Oshima, R.; Shoji, Y.; Ishizuka, S.; Müller, R.; Beutel, P.; Lackner, D.; Benick, J.; Hermle, M.; Dimroth, F.; Sugaya, T. III-V//Cu x In 1− y Ga y Se 2 Multijunction Solar Cells with 27.2% Efficiency Fabricated Using Modified Smart Stack Technology with Pd Nanoparticle Array and Adhesive Material. *Prog. Photovoltaics Res. Appl.* **2021**, *29* (8), 887−898.

(4) Yang, C.; Lunt, R. R. Limits of Visibly Transparent Luminescent Solar Concentrators. *Adv. Opt. Mater.* **2017**, *5* (8), No. 1600851.

(5) Lucas, R. M.; Yazar, S.; Young, A. R.; Norval, M.; de Gruijl, F. R.; Takizawa, Y.; Rhodes, L. E.; Sinclair, C. A.; Neale, R. E. Human Health in Relation to Exposure to Solar Ultraviolet Radiation under Changing Stratospheric Ozone and Climate. *Photochem. Photobiol. Sci.* **2019**, *18* (3), 641−680.

(6) Smith, T.; Guild, J. The C. I. E. Colorimetric Standards and Their Use. *Trans. Opt. Soc.* **1931**, *33* (3), 73−134.

(7) Hossain, M. I.; Khan, H. A.; Kozawa, M.; Qarony, W.; Salleo, A.; Hardeberg, J. Y.; Fujiwara, H.; Tsang, Y. H.; Knipp, D. Perovskite Color Detectors: Approaching the Efficiency Limit. *ACS Appl. Mater. Interfaces* **2020**, *12* (42), 47831−47839.

(8) Meiss, J.; Holzmueller, F.; Gresser, R.; Leo, K.; Riede, M. Near-Infrared Absorbing Semitransparent Organic Solar Cells. *Appl. Phys. Lett.* **2011**, *99* (19), No. 193307.

(9) Lunt, R. R.; Bulovic, V. Transparent, near-Infrared Organic Photovoltaic Solar Cells for Window and Energy-Scavenging Applications. *Appl. Phys. Lett.* **2011**, *98* (11), 113305.

(10) Chen, C.-C.; Dou, L.; Zhu, R.; Chung, C.-H.; Song, T.-B.; Zheng, Y. B.; Hawks, S.; Li, G.; Weiss, P. S.; Yang, Y. Visibly

Transparent Polymer Solar Cells Produced by Solution Processing. *ACS Nano* **2012**, *6* (8), 7185−7190.
(11) Song, Y.; Chang, S.; Gradecak, S.; Kong, J. Visibly-Transparent Organic Solar Cells on Flexible Substrates with All-Graphene Electrodes. *Adv. Energy Mater.* **2016**, *6* (20), No. 1600847.
(12) Lunt, R. R. Theoretical Limits for Visibly Transparent Photovoltaics. *Appl. Phys. Lett.* **2012**, *101* (4), No. 043902.
(13) Harayama, T.; Davis, P.; Ikeda, K. S. Nonlinear Whispering Gallery Modes. *Phys. Rev. Lett.* **1999**, *82* (19), 3803−3806.
(14) Matsko, A. B.; Ilchenko, V. S. Optical Resonators with Whispering-Gallery Modes - Part I: Basics. *IEEE J. Sel. Top. Quantum Electron.* **2006**, *12* (1), 3−14.
(15) Czekalla, C.; Nobis, T.; Rahm, A.; Cao, B.; Zúñiga-Pérez, J.; Sturm, C.; Schmidt-Grund, R.; Lorenz, M.; Grundmann, M. Whispering Gallery Modes in Zinc Oxide Micro-and Nanowires. *Phys. Status Solidi Basic Res.* **2010**, *247* (6), 1282−1293.
(16) Saleh, B. E. A.; Teich, M. C. *Fundamentals of Photonics*; 2nd ed.; Wiley, 2007; p 1200.
(17) Wang, B.; Leu, P. W. Tunable and Selective Resonant Absorption in Vertical Nanowires. *Opt. Lett.* **2012**, *37* (18), 3756−3758.
(18) *Nanophotonic FDTD Simulation Software*. Ansys Lumerical FDTD. https://www.ansys.com/products/photonics/fdtd (accessed 2023-10-10).
(19) *Particle Swarm Optimization Algorithm*. Ansys Lumerical FDTD. https://support.lumerical.com/hc/en-us/articles/360034922953-Optimization-utility (accessed 2023-10-10).
(20) Shahiduzzaman, M.; Hossain, M. I.; Visal, S.; Kaneko, T.; Qarony, W.; Umezu, S.; Tomita, K.; Iwamori, S.; Knipp, D.; Tsang, Y. H.; Akhtaruzzaman, M.; Nunzi, J.-M.; Taima, T.; Isomura, M. Spray Pyrolyzed TiO2 Embedded Multi-Layer Front Contact Design for High-Efficiency Perovskite Solar Cells. *Nano-Micro Lett.* **2021**, *13* (1), 36.
(21) Hossain, M. I.; Shahiduzzaman, M.; Ahmed, S.; Huqe, M. R.; Qarony, W.; Saleque, A. M.; Akhtaruzzaman, M.; Knipp, D.; Tsang, Y. H.; Taima, T.; Zapien, J. A. Near Field Control for Enhanced Photovoltaic Performance and Photostability in Perovskite Solar Cells. *Nano Energy* **2021**, *89*, No. 106388.
(22) Tamang, A.; Sai, H.; Jovanov, V.; Hossain, M. I.; Matsubara, K.; Knipp, D. On the Interplay of Cell Thickness and Optimum Period of Silicon Thin-Film Solar Cells: Light Trapping and Plasmonic Losses. *Prog. Photovoltaics Res. Appl.* **2016**, *24* (3), 379−388.
(23) Tamang, A.; Parsons, R.; Palanchoke, U.; Stiebig, H.; Wagner, V.; Salleo, A.; Knipp, D. Color Sensing by Optical Antennas: Approaching the Quantum Efficiency Limit. *ACS Photonics* **2019**, *6* (8), 2041−2048.
(24) Wen-Cheun Au, B.; Tamang, A.; Knipp, D.; Chan, K.-Y Post-Annealing Effect on the Electrochromic Properties of WO3 Films. *Opt. Mater.* **2020**, *108*, No. 110426.
(25) Westland, S.; Ripamonti, C.; Cheung, V. *Computational Colour Science Using MATLAB®*; Wiley, 2012.
(26) Qarony, W.; Hossain, M. I.; Tamang, A.; Jovanov, V.; Salleo, A.; Knipp, D.; Tsang, Y. H. Enhancing the Energy Conversion Efficiency of Low Mobility Solar Cells by a 3D Device Architecture. *J. Mater. Chem. C* **2019**, *7* (33), 10289−10296.
(27) Xue, Q.; Bai, Y.; Liu, M.; Xia, R.; Hu, Z.; Chen, Z.; Jiang, X. F.; Huang, F.; Yang, S.; Matsuo, Y.; Yip, H. L.; Cao, Y. Dual Interfacial Modifications Enable High Performance Semitransparent Perovskite Solar Cells with Large Open Circuit Voltage and Fill Factor. *Adv. Energy Mater.* **2017**, *7* (9), No. 1602333.
(28) Lee, K.; Um, H. D.; Choi, D.; Park, J.; Kim, N.; Kim, H.; Seo, K. The Development of Transparent Photovoltaics. *Cell Rep. Phys. Sci.* **2020**, *1* (8), No. 100143.
(29) Hossain, M. I.; Qarony, W.; Ma, S.; Zeng, L.; Knipp, D.; Tsang, Y. H. Perovskite/Silicon Tandem Solar Cells: From Detailed Balance Limit Calculations to Photon Management. *Nano-Micro Lett.* **2019**, *11* (1), 58.
(30) Shockley, W.; Queisser, H. J. Detailed Balance Limit of Efficiency of P-n Junction Solar Cells. *J. Appl. Phys.* **1961**, *32* (3), 510−519.
(31) Kirchartz, T.; Rau, U. Detailed Balance and Reciprocity in Solar Cells. *Phys. Status Solidi Appl. Mater. Sci.* **2008**, *205* (12), 2737−2751.
(32) Zhao, Y.; Yu, Y.; Gao, F. InP Nanowires Synthesized via Solvothermal Process with CTAB Assisted. *J. Cryst. Growth* **2013**, *371*, 148−154.
(33) Wallentin, J.; Anttu, N.; Asoli, D.; Huffman, M.; Åberg, I.; Magnusson, M. H.; Siefer, G.; Fuss-Kailuweit, P.; Dimroth, F.; Witzigmann, B.; Xu, H. Q.; Samuelson, L.; Deppert, K.; Borgström, M. T. InP Nanowire Array Solar Cells Achieving 13.8% Efficiency by Exceeding the Ray Optics Limit. *Science* **2013**, *339* (6123), 1057−1060.
(34) Hillerich, K.; Messing, M. E.; Reine Wallenberg, L.; Deppert, K.; Dick, K. A. Epitaxial InP Nanowire Growth from Cu Seed Particles. *J. Cryst. Growth* **2011**, *315* (1), 134−137.
(35) Krogstrup, P.; Jørgensen, H. I.; Heiss, M.; Demichel, O.; Holm, J. V.; Aagesen, M.; Nygard, J.; Fontcuberta i Morral, A. Single-Nanowire Solar Cells beyond the Shockley−Queisser Limit. *Nat. Photonics* **2013**, *7* (4), 306−310.
(36) Otnes, G.; Barrigón, E.; Sundvall, C.; Svensson, K. E.; Heurlin, M.; Siefer, G.; Samuelson, L.; Åberg, I.; Borgström, M. T. Understanding InP Nanowire Array Solar Cell Performance by Nanoprobe-Enabled Single Nanowire Measurements. *Nano Lett.* **2018**, *18* (5), 3038−3046.
(37) Borgström, M. T.; Wallentin, J.; Heurlin, M.; Fält, S.; Wickert, P.; Leene, J.; Magnusson, M. H.; Deppert, K.; Samuelson, L. Nanowires With Promise for Photovoltaics. *IEEE J. Sel. Top. Quantum Electron.* **2011**, *17* (4), 1050−1061.

https://doi.org/10.1021/acsphotonics.3c00932
ACS Photonics 2023, 10, 4205−4214